Enhanced Energy Storage with Polar Vortices in Ferroelectric Nanocomposites

Zhen Liu,[1,2] Bin Yang,[1] Wenwu Cao,[1,3,*] Edwin Fohtung,[4] and Turab Lookman[2,†]

[1]*Condensed Matter Science and Technology Institute and Department of Physics, School of Science, Harbin Institute of Technology, Harbin 150080, China*

[2]*Theoretical Division, Los Alamos National Laboratory, Los Alamos, New Mexico 87545, USA*

[3]*Materials Research Institute and Department of Mathematics, The Pennsylvania State University, University Park, Pennsylvania 16802, USA*

[4]*Experimental Physics Division, Los Alamos National Laboratory, Los Alamos, New Mexico 87545, USA*

(Received 14 April 2017; revised manuscript received 6 June 2017; published 19 September 2017)

Nanocomposites of ferroelectric ceramic filler and polymer matrix show considerable promise as high energy-storage dielectric capacitors. However, the influence of the microstructure of the ferroelectric filler on the electric energy-storage performance in the nanocomposite has not been quantitatively studied, yet it is a key element in understanding the methods employed to improve the performance of capacitors. We demonstrate a strategy to enhance the energy-storage density with topological vortex structures in nanocomposites. Using three-dimensional phase field calculations, we show that multivortex structures can exist in ferroelectric nanowires without charge defects or free charges at the interface between the filler and matrix. The switching behavior of the topological structure (vortex and antivortex pair) under external electric field is calculated in nanocylinder wires. The small remnant polarization and very narrow hysteresis loop due to the vortex structure in the nanocomposites can lead to a large enhancement of energy density, as high as 5 J/cm^3 compared to 1–2 J/cm^3 for commercial capacitors, and high energy-storage efficiency (over 95%) at a relatively low electric field of 140 MV/m.

DOI: 10.1103/PhysRevApplied.8.034014

I. INTRODUCTION

Because of the increasing demand for advanced electronic devices and electric power systems with reduced weight, size, and cost, the development of high-power and high-energy-density dielectric materials is important. The energy density of commercial dielectric capacitors is usually of the order of 1–2 J/cm^3, far inferior to electrochemical capacitors (approximately equal to 20 J/cm^3) [1]. The energy density of a dielectric material is essentially given by $U = \int EdP$, where E is the electric field and P is the polarization. Therefore, materials with large polarization value and high electric breakdown field can potentially achieve a high energy density. Unfortunately, the currently available $BaTiO_3$ and $PbZr_{1-x}Ti_xO_3$ (PZT) ferroelectric ceramics have relatively low breakdown strength. Although these materials have large polarization, the large remnant polarization (P_r) does not lead to high energy density due to the small-field-induced changes in polarization [shaded areas in Fig. 1(a)]. In high-quality ferroelectric or antiferroelectric thin films, the energy-storage density is much higher than that of ceramics due to the enhanced dielectric breakdown strength. For example, a very high energy-storage density of 154 J/cm^3 at 218 MV/m was achieved in the antiferroelectric film $(Bi_{1/2}Na_{1/2})_{0.9118}La_{0.02}Ba_{0.0582}(Ti_{0.97}Zr_{0.03})O_3$ [2], and recently, Xu *et al.* [3] predicted via first-principles calculations an energy-storage density of 100–150 J/cm^3 in the lead-free $Bi_{1-x}R_xFeO_3$ system. However, from a practical point of view, the energy density is determined by the processing method and quality of the film, as failure is often driven by flaws. The current trend in searching for high-energy-density capacitors is to use polymer-matrix composites with ferroelectric fillers, combining high dielectric permittivity of the ceramic with high breakdown strength of the polymer [4–7]. Nanowires of $Ba_{0.2}Sr_{0.8}O_3$ nanocomposites have been reported to have an energy-storage density as high as 14.86 J/cm^3 at 450 MV/m [8]. However, such large electric field strengths present a challenge to the supporting insulation systems in electronic devices, thus, limiting the applications of miniaturized devices with a high level of integration. Moreover, the remnant polarization is still a negative factor for the high energy density in the polymer nanocomposites. Therefore, it is meaningful to develop large energy-storage devices with comparable low electric field strengths. The energy utilization efficiency is another important factor for energy-storage materials and is influenced by the closed area of the hysteresis loop [9,10]. As shown in Fig. 1(b), the charged energy density (J_c) is equal to the integral area enclosed by the charge curve and the y axis, whereas the discharged energy density (J_d) is calculated by integrating the area

*Corresponding author.
dzk@psu.edu
†Corresponding author.
txl@lanl.gov

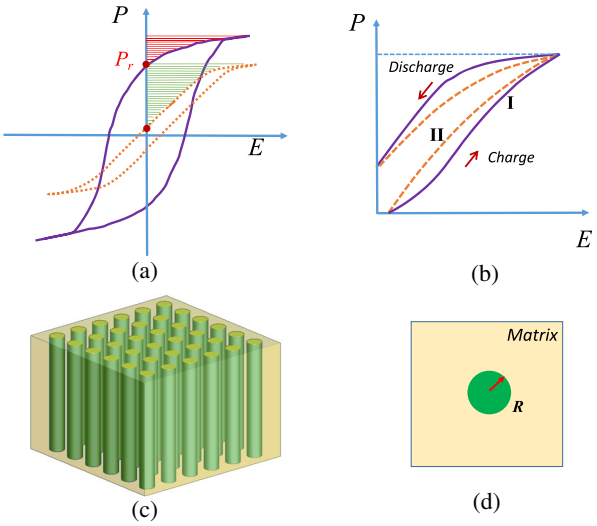

FIG. 1. (a) Schematic illustration of *P-E* hysteresis loops for the energy storage of ferroelectric materials with small remnant polarization P_r. The shaded green and red areas of the hysteresis loops indicate the available energy density. (b) Schematic illustration of the effect of the closed area of the hysteresis loops on energy-storage efficiency; the narrow *P-E* loop II compared to loop I has a larger energy-storage density and efficiency. (c) Schematic diagram of nanowire arrays embedded in nonferroelectric matrix. (d) Schematic diagram of the model of the nanowire with a radius R in the matrix in the simulation.

enclosed by the discharge curve and the y axis. The energy-storage efficiency is J_d/J_c. Thus, a narrow hysteresis loop contributes to higher energy-storage efficiency. The microstructure of the ferroelectric filler plays an important role in the dielectric property and electric energy density, but its influence on enhancing electric energy storage has been little studied and forms the focus of this work. The shape of fillers, charge defects, and the inner stresses can affect the microstructure of the ferroelectric nanocomposite, thus, impacting the electric energy storage and ultimately the design and optimization. We focus here on exploring the effects of polarization vortices on properties of ferroelectric composites.

The vortex domain structure has been observed in ferroelectric nanoparticles [11,12], and polar vortices in superlattices demonstrated in Ref. [13] have been directly observed recently in $PbTiO_3/SrTiO_3$ superlattices [14], although nonuniform domain morphologies were studied using an electrostatic model in Ref. [15]. The vortex-to-polarization phase transition in $Pb(ZrTi)O_3$ nanoparticles [16] was predicted on the basis of *ab initio* calculations. Thereafter, vortex states with geometrical textures and critical temperatures were studied in two-dimensional systems [17]. In ferroelectric nanowires (NWs), the vortex structure has also been inferred via first-principles calculations [18]. A vortex core transition and phase locking of ferroelectric vortices accompanied by the formation of antivortices was predicted in $BaTiO_3/SrTiO_3$ nanocomposites [19] using first-principles calculations. A three-dimensional phase field study of domain structure in ferroelectric nanorods of different shapes and sizes was carried out by Slutsker *et al.* [20].The possible applications of topological defects in electronic devices were investigated in the past decade [21–23]. Experimentally, electric conductivity was explored to be enhanced at the vortex cores in $BiFeO_3$ [21], which is related to a form of modified band alignment as predicted by *ab initio* calculations [23]. Topologically, the ferroelectric vortex phase is expected to increase the information-storage density by 5 orders of magnitude in memory devices [22]. In this work, we show that in nanocomposites with $BaTiO_3$ embedded in a nonferroelectric polymer matrix, a topological vortex and antivortex phase can coexist if no free charges are present at the interface between the filler NWs and the matrix. This vortex structure undergoes a very different phase transition from that observed in common nonlinear dielectric materials. It leads to an almost zero remnant polarization P_r and a very narrow polarization-electric (*P-E*) hysteresis loop, resulting in a large energy-storage density and efficiency even at relatively low electric fields. This finding provides us with an approach to enhance the electric energy storage of dielectric capacitors.

II. THEORETICAL MODEL

The microstructure and dielectric property of nanocomposites can be calculated by employing phase field simulations based on mesoscale Landau theory in which the phase structure is described by the distribution of polarization $\mathbf{P}(\mathbf{r})$. To model the ferroelectric NW arrays embedded in the nonferroelectric polymer matrix as shown in Fig. 1(c), we simulate the evolution of the polarization in the NWs while maintaining a fixed polarization $\mathbf{P} \approx \varepsilon_m \varepsilon_0 \mathbf{E}$ for different external electric fields $\mathbf{E}$ in the matrix, where ε_0 is the vacuum dielectric permittivity, and ε_m denotes the permittivity of the matrix material. We assume that the system is free of charge defects, and no space charges exist at the interface between the ferroelectric filler and the dielectric matrix. The equilibrium state is described by the polarization distribution corresponding to the minimum free-energy state. The total free energy of the NWs can be written as [24]

$$F = \int d^3r \left[f(\mathbf{P}) + \frac{1}{2}\beta_{ijkl}\nabla_i P_j \nabla_k P_l - \mathbf{E}\cdot\mathbf{P} \right] + \frac{1}{2}\int \frac{d^3k}{(2\pi)^3}\left[\frac{k_i k_j}{\varepsilon_0 \varepsilon_b k^2}\tilde{P}_i \tilde{P}_j^* + K_{ijkl}\tilde{\varepsilon}_{ij}^0 \tilde{\varepsilon}_{kl}^{0*} \right], \quad (1)$$

where

$$f(\mathbf{P}) = \alpha_1(P_1^2 + P_2^2 + P_3^2) + \alpha_{11}(P_1^4 + P_2^4 + P_3^4) + \alpha_{12}(P_1^2P_2^2 + P_2^2P_3^2 + P_3^2P_1^2) + \alpha_{111}(P_1^6 + P_2^6 + P_3^6) + \alpha_{112}[P_1^4(P_2^2 + P_3^2) + P_2^4(P_1^2 + P_3^2) + P_3^4(P_1^2 + P_2^2)] + \alpha_{123}P_1^2P_2^2P_3^2 \quad (2)$$

is the Landau-Devonshire free-energy density, and α_1, α_{11}, α_{111}, α_{12}, α_{112}, α_{123} are the Landau coefficients. The gradient term in Eq. (1) denotes the energy contribution from the polarization changes in the NW and interfaces, $\nabla_i = \partial/\partial_i$ is the gradient operator, and β_{ijkl} is the gradient coefficient. The $\mathbf{k}$-space integral in Eq. (1) represents the electrostatic energy and the elastostatic energy, in which ε_0 and ε_b are the permittivity of vacuum and background permittivity of the material, respectively. $K_{ijkl} = C_{ijkl} - n_m C_{ijmn}\Omega_{np}C_{klpq}n_q$, $\Omega_{ik} = (C_{ijkl}n_jn_l)^{-1}$, C_{ijkl} is the elastic stiffness constant tensor, and $\mathbf{n} = \mathbf{k}/k$ is the unit wave vector. The spontaneous strain ε_{ij}^0 is given by $\varepsilon_{ij}^0 = Q_{ijkl}P_kP_l$, where Q_{ijkl} is the electrostrictive coefficient. The elastic moduli are assumed to be equal in the nanowires and matrix. In Eq. (1), $\tilde{P}_i$ and $\tilde{\varepsilon}_{ij}^0$ are the Fourier transforms of P_i and ε_{ij}^0. The temporal evolution of the polarization can be obtained by solving the time-dependent Ginzburg-Landau equation [25]:

$$\frac{\delta P_i(\mathbf{r},t)}{\delta t} = -L\frac{\delta F}{\delta P_i(\mathbf{r},t)}, \qquad (i = 1,2,3), \quad (3)$$

where L is the kinetic coefficient. In our phase field simulation, a $40 \times 40 \times 128$ grid with 4.24-nm spatial steps is used to simulate the NW embedded in a dielectric matrix. The core part is the infinite cylindrical NW with a radius R, while the outer part is the nonferroelectric medium in Fig. 1(d). Periodic boundary conditions are used in all three axial directions to model the infinite NW arrays in the matrix. The Landau parameters are taken from Ref. [26]. The elastic constants $C_{11} = 17.8 \times 10^{10}$ N/m^2, $C_{12} = 9.6 \times 10^{10}$ N/m^2, and $C_{44} = 12.2 \times 10^{10}$ N/m^2, the electrostrictive constants are $Q_{11} = 0.11$ m^4/C^2, $Q_{12} = -0.034$ m^4/C^2, and $Q_{44} = 0.059$ m^4/C^2, the background permittivity ε_b is set as 100 in ferroelectric NWs, and $\varepsilon_m = 3$ in dielectric matrix.

III. RESULTS AND DISCUSSION

The mechanism for the formation of vortex domains is the competition between the elastic energy, the electrostatic energy, and the gradient energy. The elastic energy, which arises from the fact that $BaTiO_3$ NWs are constrained by the nonferroelectric polymer matrix, drives the NWs to adopt a mixture of in-plane P_x, P_y and out-of-plane P_z polarizations. The second major contribution is the electrostatic energy induced by the built-in electric fields. If the interface between the ferroelectric NWs and the nonferroelectric matrix is charge-free or has a very small charge density, i.e., $\nabla \cdot \mathbf{P} \approx 0$, the polarizations tend to align parallel to the interface. Finally, the gradient energy tends to change the direction and magnitude of the polarization. The three energy contributions lead to the topological structure in the NWs. The domain structure of the NW is visualized by color maps in red, green, and blue for components P_x, P_y, and P_z, respectively, as shown in Fig. 2(a) (plotting details are given in the Supplemental Material [27]), and the colored arrows represent the in-plane polarization distribution P_x, P_y corresponding to the vortex structures in Fig. 2(a). Unlike the reported multivortex structures in nanogeometries confined in a two-dimensional

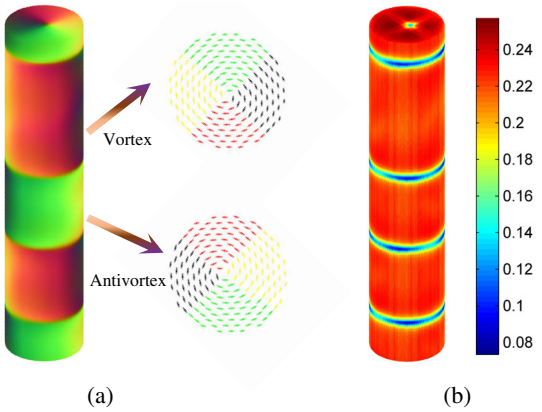

FIG. 2. Topological domain structures in the nanowire. (a) The domain structure of the NW is visualized by color maps in red, green, and blue for components P_x, P_y, and P_z; the colored arrows denote the in-plane polarization directions P_x, P_y; vortex and antivortex domains coexist in the nanowire. (b) The distribution of the magnitude of polarization in the nanowire.

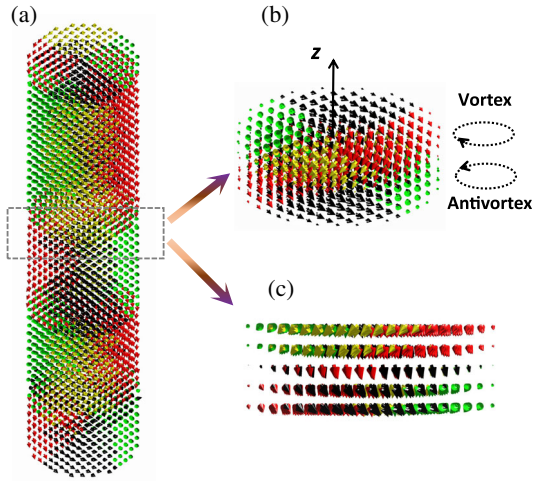

FIG. 3. (a) Polarization distribution in the $R = 22.4$ nm NW. (b),(c) The polarization changes across the domain wall.

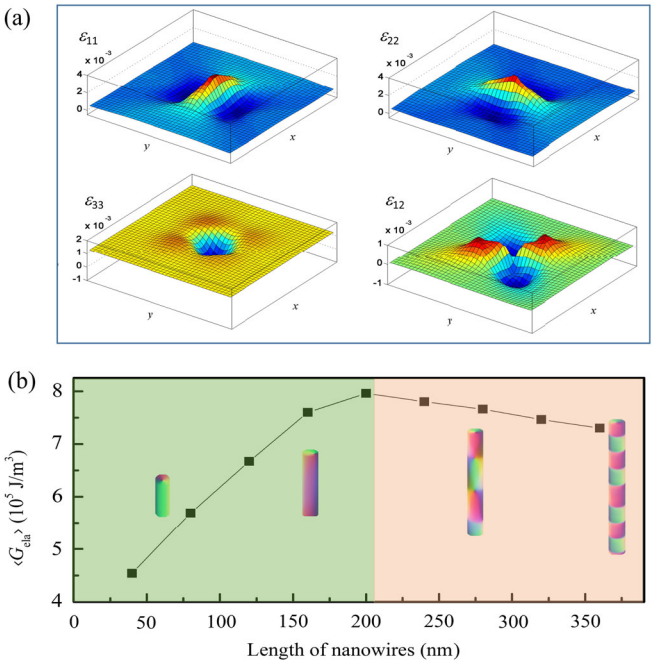

FIG. 4. (a) The distribution of the total strain ε_{11}, ε_{22}, ε_{33}, and ε_{12} in the top plane of the NW. (b) The average total elastic energy density $\langle G_{ela} \rangle$ with the length of the NWs. $\langle G_{ela} \rangle$ increases with the length of the NW, and the multivortex structure exists in order to decrease the elastic energy.

plane [17], the vortex (in the clockwise direction) and antivortex (counterclockwise direction) structures coexist along the axis of the $R = 22.4$ nm NW in the absence of an external electric field but not in the same plane. Figure 2(b) shows the magnitude of the polarization in the NW. The blue color in the center of the NW represents the vortex core, and the blue bands on the wire indicate the domain walls that separate the vortex and antivortex domains. The spontaneous polarization of the vortex domain in the ferroelectric NWs is about 0.24 C/m^2. The exact distribution of the polar vector $P(P_x, P_y, P_z)$ is shown in Fig. 3(a), and the in-plane polarization P_x, P_y forms the vortex-antivortex structures, while there is a polarization component P_z out of plane along the z axis. Figures 3(b) and 3(c) show clearly that the polarization changes across the vortex-antivortex domain wall shown by the dashed rectangular region in Fig. 3(a). The arrows at the domain wall denote the small magnitude of polarization corresponding to Fig. 2(b).

Figure 4(a) shows the components of the total elastic strain tensor, that is, ε_{11}, ε_{22}, ε_{33}, and ε_{12} in the top plane of the NW. The patterns of the strain components are similar to that of first-principles calculations in PZT nanodots [28] with large values of ε_{11}, ε_{22} near the vortex core. However, the magnitude of the strains are smaller in the NW case due to the constraint of the matrix and smaller spontaneous polarization of $BaTiO_3$. The symmetry of the ε_{12} strain pattern together with ε_{11}, ε_{22} can guide experiments towards finding topological vortices in ferroelectric nanowires. The reason for the existence of the vortex-antivortex pair is due to the competition between the gradient energy and elastic energy. The multivortex structure will increase the gradient energy due to changes in polarization across the domain wall, but it will decrease the total elastic energy. For $R = 22.4$ nm NWs with short length, a single vortex exists as the gradient energy is the principal contributor. The average elastic energy density $\langle G_{ela} \rangle$ is obtained from $\langle G_{ela} \rangle = [(F_{ela})/V]$, where F_{ela} is the total elastic energy, and V is the volume of the NW. The energy $\langle G_{ela} \rangle$ increases with length below 200 nm, as shown in Fig. 4(b). Above 200 nm, if no transition occurs from single vortex to multivortex in the nanowire, then $\langle G_{ela} \rangle$ continues increasing. Thus, the elastic energy is a major contributor in the transition from single vortex to multivortex structures in order to decrease the elastic energy (see Fig. S4 in the Supplemental Material [27]). The decreasing of $\langle G_{ela} \rangle$ in Fig. 4(b) above 200 nm is accompanied by an increase in the number of vortex-antivortex pairs.

In order to investigate the dielectric response, we apply an external electric field along the y axis to study the dynamic properties of the vortex domains in the NWs. This is shown in Fig. 5 for the NW with $R = 22.4$ nm. The vortex center is along the axis of the NW at zero applied electric field in Fig. 5(a). With increasing electric field, the vortex and antivortex display reverse switching behavior: The antivortex center moves towards the negative x direction, whereas the vortex moves towards the opposite direction, as shown in Fig. 5(b). When the electric field is large enough at 110.9 MV/m, both the vortex and antivortex structures switch to a single-domain phase with polarization along the [010] direction, as shown in Fig. 5(c). In order to show the vortex movement inside the NWs, the magnitude of the polarization distribution in the $y = 0$ plane is calculated. In Fig. 5(e), the vortex core (blue color) acts as a line defect, usually regarded as an Ising line [29], in the center of the NW at zero field. At a field value of $E = 55.4$ MV/m, as shown in Fig. 5(f), the Ising line passing through the vortex and antivortex cores separates into two parts, one associated with the vortices and the other with the antivortices. However, when the field decreases to zero, the vortex and antivortex structures reappear as show in Fig. 5(d), and the average polarization along the field direction [010] is zero in the vortex. Thus, macroscopically, this state corresponds to a zero remnant polarization of the nanocomposite capacitor. Figure 5(g) depicts the normalized average polarization along [010] and the toroidal moment $\mathrm{TM} = [1/(\mathrm{TM}_0)] \int \mathbf{r} \times \mathbf{P}$ as a function of the electric field, where TM_0 denotes the value of the toroidal moment without field. The polarization along [010] increases with the electric field, whereas the toroidal moment decreases with the field. At $E = 75$ MV/m, the zero value of TM indicates a special vortex-to-polarization phase transformation in the ferroelectric NW.

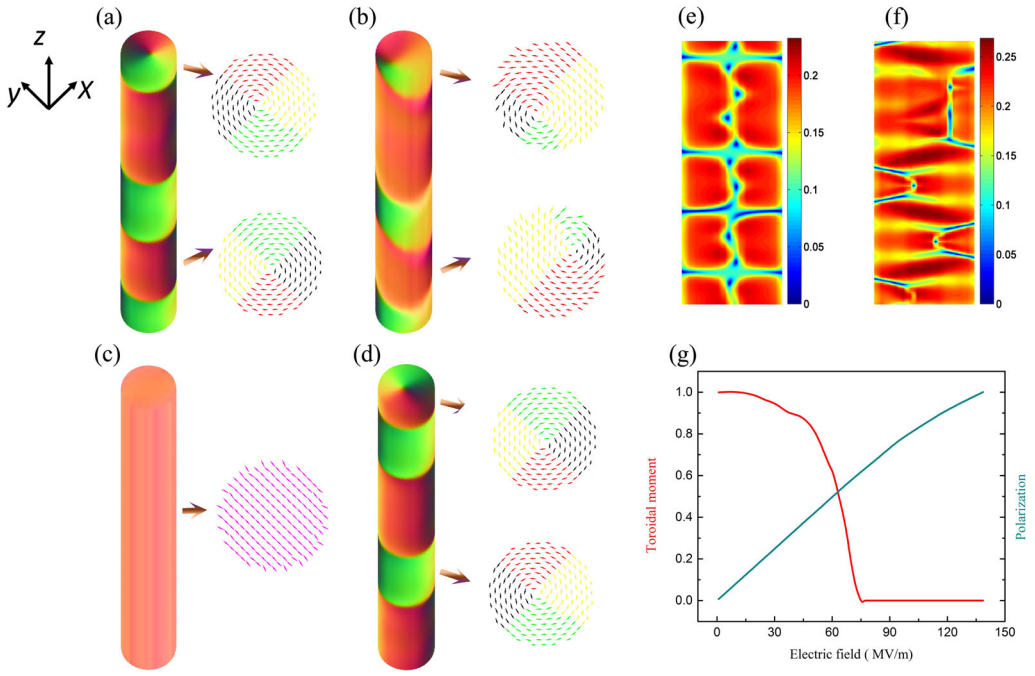

FIG. 5. The dynamic behavior of the vortex structure under an external electric field along the [010] direction. (a)–(d) show the domain switching with increasing electric field. (a) $E = 0$, the vortex core is along the axis of the NWs; (b) $E = 55.4$ MV/m, the vortex and antivortex display reverse switching behavior, and the cores of the vortex and antivortex move to the edge of the NWs but in opposite direction along the x axis. (c) $E = 110.9$ MV/m, the domains are poled to a single domain along [010], and the topological structures disappear. (d) The vortex structure appears again with the electric field decreasing to zero. (e),(f) show the topological core lines of the vortex structure across the inner lengthwise cross section of the nanowire at $E = 0$ and $E = 55.4$ MV/m, respectively. (g) The average polarization along the field direction and the behavior of the toroidal moment vs the field.

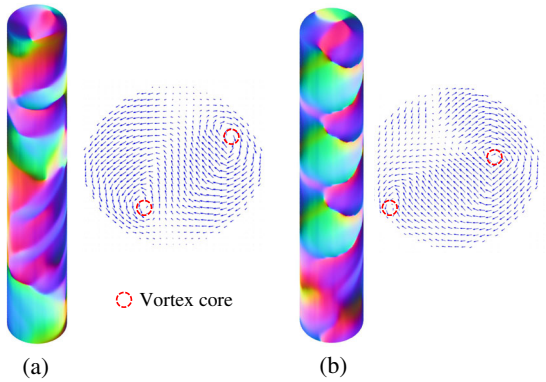

FIG. 6. Domain distribution of NWs with a radius of 57 nm; two vortices exist on certain cross sections of the NW, and the arrows show the polarization distribution on the top plane. (a) The unpoled domain structure. (b) The poled domain structure.

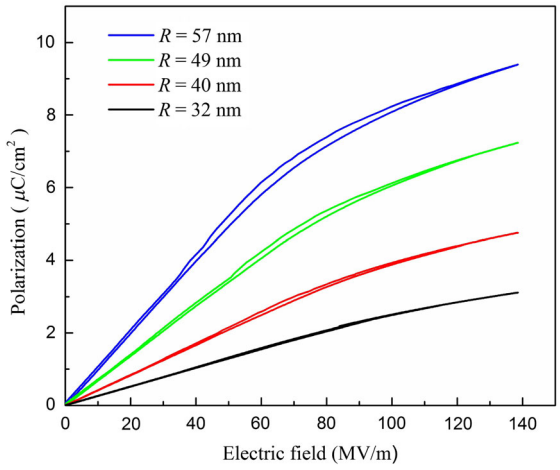

FIG. 7. The calculated P-E loop with increasing the radius R of the NWs.

Since the vortex structure is sensitive to the size of the NW, we carry out several simulations with increasing NW radius R. If $R = 57$ nm, the resulting domain structure is no longer regular as previously described. The structures for the NW are now far more complex, as shown in Figs. 6(a) and 6(b), where the blue arrows denote the in-plane polarization at the top face of the NW. A vortex-antivortex pair can now coexist in one plane.

The electrical hysteresis loops for different NW R values are calculated in Fig. 7. As R increases from 32 to 57 nm, the saturation polarization increases from 3 to about 10 μC/cm^2. Compared to the hysteresis loop for bulk $BaTiO_3$ [30], our NW $BaTiO_3$ nanocomposites have an almost zero remnant polarization due to the vortex structure and much slimmer hysteresis loops. Thus, the almost zero

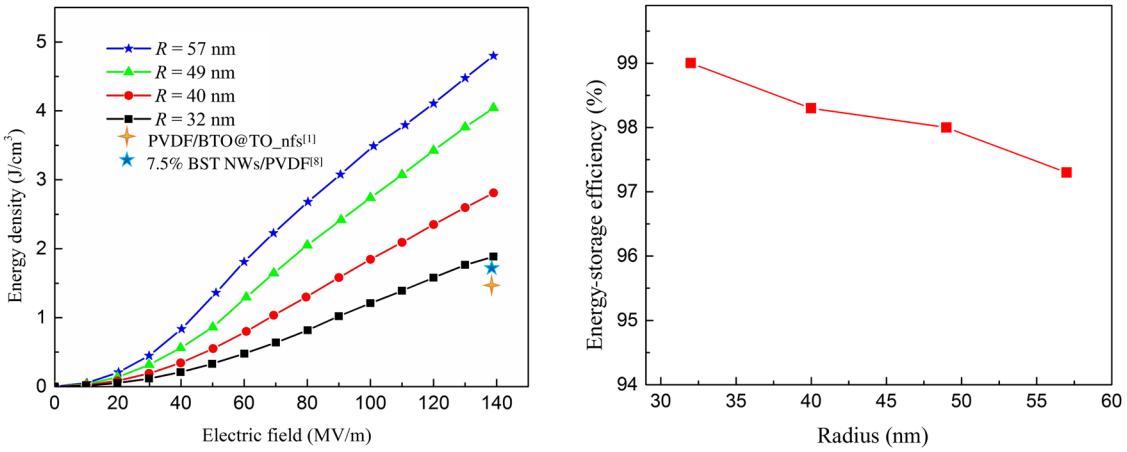

FIG. 8. (a) The calculated energy-storage density with increasing the radius R of the NWs. At a relatively low electric field of about 140 MV/m, the energy density can reach as high as 5 J/cm^3 compared to 1.5 J/cm^3 of recently reported nanocomposite materials. (b) The calculated energy-storage efficiency vs the radius R.

remnant polarization and very small closed area of the P-E loops associated with the topological structures lead to considerable enhancement of the energy density in our NW composites. The exact energy-storage densities as a function of increasing R from 32 to 57 nm are shown in Fig. 8(a). The energy density increases from 1.8 to 5.0 J/cm^3 at 140 MV/m as R increases. The reported energy density for the nanocomposites with $BaTiO_3$ nanoparticles embedded in TiO_2 nanofibers in polyvinylidene fluoride matrix (PVDF/BTO@TO_nfs) is about 1.4 and 1.7 J/cm^3 for the 7.5% $Ba_{0.2}Sr_{0.8}TiO_3$ NWs in polyvinylidene fluoride nanocomposites at the same field [1,8,31] [see Fig. 8(a)]. The enhancement of the energy density is about threefold due to the polar vortex structures. Figure 8(b) shows the calculated energy-storage efficiency; with the increasing of the radius R, the energy efficiency decreases. However, the efficiency is over 95% at $R = 57$ nm, which is higher than that of the reported $BaTiO_3$@$SrTiO_3$ ceramics (about 90%) [9].

IV. CONCLUSIONS

In conclusion, we study the dielectric properties of cylindrical nanowire composites consisting of ferroelectric filler in a polymer matrix with coexisting vortex and antivortex structures using phase field simulations. The special vortex-to-polarization phase transformation under an electric field leads to an almost zero remnant polarization and a very slim hysteresis loop, which significantly enhances the energy density and efficiency in the nanocomposites. Even at a relatively low electric field of 140 MV/m, the energy density can reach as high as 5 J/cm^3 compared to 1.5 J/cm^3 of recently reported nanocomposite materials, and the energy efficiency is above 95%. Our results suggest an alternate strategy to improve the electrical energy storage in composite dielectric capacitors. Experimentally, oxygen vacancies or other charge defects in the ferroelectric NWs can potentially affect the formation of topological vortex structures. Hence, our work should motivate experiments to further decrease concentrations of defects and free charges at interfaces between ferroelectric fillers and matrices to produce dielectric capacitors with enhanced energy-storage capacity.

ACKNOWLEDGMENTS

The work is supported by the National Key Basic Research Program of China (Grant No. 2013CB632900), the State Scholarship Fund of the China Scholarship Council (Grant No. 201506120195), and Los Alamos National Laboratory.

[1] Xin Zhang, Yang Shen, Qinghua Zhang, Lin Gu, Yuhan Hu, Jiawen Du, Yuanhua Lin, and Ce-Wen Nan, Ultrahigh energy density of polymer nanocomposites containing $BaTiO_3$@TiO_2 nanofibers by atomic-scale interface engineering, Adv. Mater. **27**, 819 (2015).

[2] Biaolin Peng, Qi Zhang, Xing Li, Tieyu Sun, Huiqing Fan, Shanming Ke, Mao Ye, Yu Wang, Wei Lu, Hanben Niu, James F. Scott, Xierong Zeng, and Haitao Huang, Giant electric energy density in epitaxial lead-free thin films with coexistence of ferroelectrics and antiferroelectrics, Adv. Electron. Mater. **1**, 1500052 (2015).

[3] Bin Xu, Jorge Íñiguez, and L. Bellaiche, Designing lead-free antiferroelectrics for energy storage, Nat. Commun. **8**, 1500052 (2017).

[4] Junjun Li, Jason Claude, Luis Enrique Norena-Franco, Sang Il Seok, and Qing Wang, Electrical energy storage in ferroelectric polymer nanocomposites containing

surface-functionalized $BaTiO_3$ nanoparticles, Chem. Mater. **20**, 6304 (2008).

[5] Junjun Li, Sang Il Seok, Baojin Chu, Fatih Dogan, Qiming Zhang, and Qing Wang, Nanocomposites of ferroelectric polymers with TiO_2 nanoparticles exhibiting significantly enhanced electrical energy density, Adv. Mater. **21**, 217 (2009).

[6] Xingyi Huang and Pingkai Jiang, Core-shell structured high-k polymer nanocomposites for energy storage and dielectric applications, Adv. Mater. **27**, 546 (2015).

[7] Ke Yang, Xingyi Huang, Yanhui Huang, Liyuan Xie, and Pingkai Jiang, Fluoro-polymer@$BaTiO_3$ hybrid nanoparticles prepared via RAFT polymerization: Toward ferroelectric polymer nanocomposites with high dielectric constant and low dielectric loss for energy storage application, Chem. Mater. **25**, 2327 (2013).

[8] Haixiong Tang and Henry A. Sodano, Ultra high energy density nanocomposite capacitors with fast discharge using $Ba_{0.2}Sr_{0.8}TiO_3$ nanowires, Nano Lett. **13**, 1373 (2013).

[9] Longwen Wu, Xiaohui Wang, Huiling Gong, Yanan Hao, Zhengbo Shen, and Longtu Li, Core-satellite $BaTiO_3$@$SrTiO_3$ assemblies for a local compositionally graded relaxor ferroelectric capacitor with enhanced energy storage density and high energy efficiency, J. Mater. Chem. C **3**, 750 (2015).

[10] Sheng Tong, Beihai Ma, Manoj Narayanan, Shanshan Liu, Rachel Koritala, Uthamalingam Balachandran, and Donglu Shi, Lead lanthanum zirconate titanate ceramic thin films for energy storage, ACS Appl. Mater. Interfaces **5**, 1474 (2013).

[11] Alexei Gruverman, D. Wu, H. J. Fan, I. Vrejoiu, M. Alexe, R. J. Harrison, and J. F. Scott, Vortex ferroelectric domains, J. Phys. Condens. Matter **20**, 342201 (2008).

[12] B. J. Rodriguez, X. S. Gao, L. F. Liu, W. Lee, I. I. Naumov, A. M. Bratkovsky, D. Hesse, and M. Alexe, Vortex polarization states in nanoscale ferroelectric arrays, Nano Lett. **9**, 1127 (2009).

[13] Pavlo Zubko, N. Jecklin, Almudena Torres-Pardo, P. Aguado-Puente, A. Gloter, Céline Lichtensteiger, J. Junquera, O. Stéphan, and J.-M. Triscone, Electrostatic coupling and local structural distortions at interfaces in ferroelectric/paraelectric superlattices, Nano Lett. **12**, 2846 (2012).

[14] A. K. Yadav, C. T. Nelson, S. L. Hsu, Z. Hong, J. D. Clarkson, C. M. Schlepütz, A. R. Damodaran, P. Shafer, E. Arenholz, L. R. Dedon, D. Chen, A. Vishwanath, A. M. Minor, L. Q. Chen, J. F. Scott, L. W. Martin, and R. Ramesh, Observation of polar vortices in oxide superlattices, Nature (London) **530**, 198 (2016).

[15] F. De Guerville, I. Lukyanchuk, L. Lahoche, and M. El Marssi, Modeling of ferroelectric domains in thin films and superlattices, Mater. Sci. Eng. B **120**, 16 (2005).

[16] Ivan Naumov and Huaxiang Fu, Vortex-to-Polarization Phase Transformation Path in Ferroelectric $Pb(ZrTi)O_3$ Nanoparticles, Phys. Rev. Lett. **98**, 077603 (2007).

[17] L. Lahoche, I. Luk'Yanchuk, and G. Pascoli, Stability of vortex phases in ferroelectric easy-plane nano-cylinders, Integr. Ferroelectr. **99**, 60 (2008).

[18] G. Pilania and R. Ramprasad, Complex polarization ordering in $PbTiO_3$ nanowires: A first-principles computational study, Phys. Rev. B **82**, 155442 (2010).

[19] Lydie Louis, Igor Kornev, Grégory Geneste, Brahim Dkhil, and L. Bellaiche, Novel complex phenomena in ferroelectric nanocomposites, J. Phys. Condens. Matter **24**, 402201 (2012).

[20] J. Slutsker, A. Artemev, A. Roytburd, Phase-Field Modeling of Domain Structure of Confined Nanoferroelectrics, Phys. Rev. Lett. **100**, 087602 (2008).

[21] Nina Balke, Benjamin Winchester, Wei Ren, Ying Hao Chu, Anna N. Morozovska, Eugene A. Eliseev, Mark Huijben, Rama K. Vasudevan, Petro Maksymovych, Jason Britson, Stephen Jesse, Igor Kornev, Ramamoorthy Ramesh, Laurent Bellaiche, Long Qing Chen, and Sergei V. Kalinin, Enhanced electric conductivity at ferroelectric vortex cores in $BiFeO_3$, Nat. Phys. **8**, 81 (2012).

[22] Ivan I. Naumov, L. Bellaiche, and Huaxiang Fu, Unusual phase transitions in ferroelectric nanodisks and nanorods, Nature (London) **432**, 737 (2004).

[23] Zhigang Gui, Lin-Wang Wang, and L. Bellaiche, Electronic properties of electrical vortices in ferroelectric nanocomposites from large-scale *ab initio* computations, Nano Lett. **15**, 3224 (2015).

[24] Wei-Feng Rao and Yu U. Wang, Domain wall broadening mechanism for domain size effect of enhanced piezoelectricity in crystallographically engineered ferroelectric single crystals, Appl. Phys. Lett. **90**, 041915 (2007).

[25] Zhen Liu, Bin Yang, Wenwu Cao, and Turab Lookman, Effect of misfit strain on ferroelectric domain formation at the morphotropic phase boundary, Phys. Rev. B **94**, 214117 (2016).

[26] Tomas Sluka, Alexander K. Tagantsev, Dragan Damjanovic, Maxim Gureev, and Nava Setter, Enhanced electromechanical response of ferroelectrics due to charged domain walls, Nat. Commun. **3**, 748 (2012).

[27] See Supplemental Material at http://link.aps.org/supplemental/10.1103/PhysRevApplied.8.034014 for the plotting details of domain structures in the nanowires.

[28] S. Prosandeev and L. Bellaiche, Characteristics and signatures of dipole vortices in ferroelectric nanodots: First-principles-based simulations and analytical expressions, Phys. Rev. B **75**, 094102 (2007).

[29] V. Stepkova, P. Marton, and J. Hlinka, Ising lines: Natural topological defects within ferroelectric Bloch walls, Phys. Rev. B **92**, 094106 (2015).

[30] H. Basantakumar Sharma, H. N. K. Sarma, and A. Mansingh, Ferroelectric and dielectric properties of sol-gel processed barium titanate ceramics and thin films, J. Mater. Sci. **34**, 1385 (1999).

[31] Penghao Hu, Yang Shen, Yuhan Guan, Xuehui Zhang, Yuanhua Lin, Qiming Zhang, and Ce-Wen Nan, Topological-structure modulated polymer nanocomposites exhibiting highly enhanced dielectric strength and energy density, Adv. Funct. Mater. **24**, 3172 (2014).